Interaction between the diffusion layer and the flow field of polymer electrolyte fuel cells—experiments and simulation studies

H. Dohle*, R. Jung, N. Kimiaie, J. Mergel, M. Müller

Institut für Werkstoffe und Verfahren der Energietechnik (IWV-3) Forschungszentrum Jülich GmbH, D-52425 Jülich, Germany

Abstract

The flow distribution in fuel cells has an important influence on both the power density and efficiency of fuel cell systems. In order to effectively utilize the area, flow distribution should be as homogeneous as possible. In addition, pressure losses should be minimized with regard to the power demand of auxiliary components as pumps and compressors. In polymer electrolyte fuel cells (PEFCs) and direct methanol fuel cells (DMFCs) the flow field is in direct contact with the diffusion layer. The main task of the diffusion layer is to distribute the reactants from the flow field towards the catalyst layer. To prevent diffusion overvoltages, the diffusion layer is in general highly porous and provides high fluxes of the reactants. Consequently, the flow distribution in the flow field can be superpositioned by a flow in the diffusion layer. In this paper, we discuss the interaction between the diffusion layer and the flow field. Experimentally, we characterized different diffusion layers with regard to their diffusion properties as well as different flow fields. Additional simulation studies help to understand the processes and to determine suitable combinations of flow fields and diffusion layers.
© 2003 Elsevier B.V. All rights reserved.

Keywords: Diffusion layer; Polymer electrolyte; Fuel cells

1. Introduction

Fuel cells are promising energy converters since the efficiency achievable is higher than in power plants or internal combustion engines.

The bipolar plates in fuel cell stacks have to fulfill various requirements such as homogeneous flow distribution, current transport and product water removal. Furthermore, the bipolar plates are in direct contact with the membrane electrode assemblies (MEAs) so that they have to be highly conductive and chemically inert. For economic reasons and due to market demands, they are required to be light-weight and to be manufactured at low costs.

In particular PEFCs are interesting for automotive and portable applications because of their low operating temperature. In this cell types, the cathodes have a great impact on the performance of the cell. To reduce the energy demand of the auxiliary components such as compressors or pumps, the flow rate and the pressure drop should be as low as possible. The basic processes of both PEM and DMFC fuel cells are shown in Fig. 1. In addition to the electrochemical oxidation and reduction processes the performance of the

DMFC is affected by the methanol permeation from the anode to the cathode where the methanol is chemically oxidized. Although PEM and DMFC have similar theoretical open circuit voltages E_0 (Table 1) the methanol permeation lowers the DMFC cell voltage by several hundreds of mV.

Generally, a fuel cell stack consists of several single cells connected in series by bipolar plates. In the same time, the flow fields of the bipolar plates provide the MEAs with reactants. Fig. 2 gives a more detailed view inside a single cell. Each flow field is in direct contact with the membrane electrode assembly which consists of the catalyst coated proton conducting membrane and the diffusion layers. To provide high fluxes of reactants towards the catalyst layer the diffusion layers are highly porous. In addition, product water removal is made by a fraction of hydrophobic pores which is dependent on the PTFE content inter alia. The task of the flow field is to provide a homogeneous distribution of the reactants on the whole cell area. An effective use of the whole flow field is important with regard to the power output, the specific volumetric power density and at least the utilization of the catalyst layer. DMFC stacks in the power range from several watts to the kW class have recently been reported [1–3].

In addition to the flow homogeneity, the pressure drop from the inlet manifold to the outlet should be as low as

---

* Corresponding author. Fax: +49-2461-61-6695.
E-mail address: h.dohle@fz-juelich.de (H. Dohle).

Nomenclature

a	anode
A_{cell}	cell area (m^2)
A_{mem}	active area of the single cell (m^2)
A_M	cross-sectional area of the meander channel (m^2)
b_M	width of the meander channel (m)
c	cathode
c_{MeOH}	methanol concentration (mol/l)
d_{hyd}	hydraulic diameter (m)
E_0	open circuit voltage (V)
F	Faraday constant 96,485 As/mol
h_M	height of the meander channel (m)
in	at the inlet
I	cell current (A)
k	permeability (m^2)
$\bar{\bar{L}}$	coupling matrix
L_M	length of the meander (m)
M_{air}	air mass 28.96 kg/mol
N	number of parallel channels
out	at the outlet
p	pressure (bar)
$\bar{p}$	vector containing the local pressures
r	radius (m)
R_{in}	inner diameter (m)
R_{out}	outer diameter (m)
Re	Reynold's number
s	gap width (m)
U_M	circumfence of the meander channel (m)
v_{diff}	flow velocity in the diffusion layer (m^2)
$\bar{v}_{spec}$	specific volume flow ($m^3/m^2 s$)
$\dot{V}$	volume flow (m3/s)
x	molar fraction (mol/mol)

Greek letters

χ	fraction
η	dynamic viscosity (kg/ms)
λ	stoichiometric flow factor
ν	kinematic viscosity $= \eta/\rho$ (Pa s)
ρ	density (kg/m^3)
ψ	flow homogeneity

possible because of the power consumption of the auxiliary components (e.g. of the air compressor).

Different flow field structures are well known for PEM and DMFC fuel cells (Fig. 3) [4–8]. In principle, the channel structure offers a homogeneous flow distribution with low pressure drops. But on the other hand the formation of liquid water droplets at the cathode can flood one or more channel with the consequence of stopping the gas flow there. In previous measurements with 100 cm^2 laboratory test cells we observed channel flooding after a certain time of constant operation (approximately 10 min) which leads directly to a voltage decrease. The decrease can be stopped only by removing the water frequently from the channels by purging the cathode [6]. In single cells this may not be a problem, but in stacks the probability of channels being blocked by water droplets is elevated simply due to the increased number of cells. This requires more often compressor power consuming purging procedures affecting the overall efficiency.

Therefore, special attention must be drawn to a flow field with no flooding effects and low pressure drops.

With regard to the flooding the interdigitated structure is beneficial. The flow is pressed from the inlet to the outlet directly through the diffusion layer. This structure provides also the regions of the catalyst layer which are situated underneath the rib with sufficient amounts of reactants. As a drawback, the pressure drop from the inlet to the outlet is relatively high [4,6].

The third flow field (c) shown in Fig. 3 is the meander structure where one or more parallel meanders guide the flow across the active area of the membrane-electrode-assembly. Increasing the number of meander channels decreases the pressure drop because the total volume flow is distributed and the length of each meander decreases with their number, but on the other hand too many meanders lead to the same situation described for the parallel channel flow field, i.e. partially meander channels can be blocked by water droplets.

1.1. Flow interaction between the diffusion layer and the flow field

In both PEM and DMFC fuel cells the flow field is in direct contact with the diffusion layer which distributes the reactants from the flow field towards the catalyst layer. To avoid diffusion overvoltages the diffusion layer is in general highly porous and provides high fluxes of the reactants. Consequently, the flow distribution in the flow field can be superpositioned by a flow in the diffusion layer which is schematically indicated in Fig. 4. In this paper, we focus on the flow interaction mainly in meander structures.

In the following the different approaches for our study are described. In experiments simulating the processes in

Table 1
Reactions and voltages of PEM and DMFC

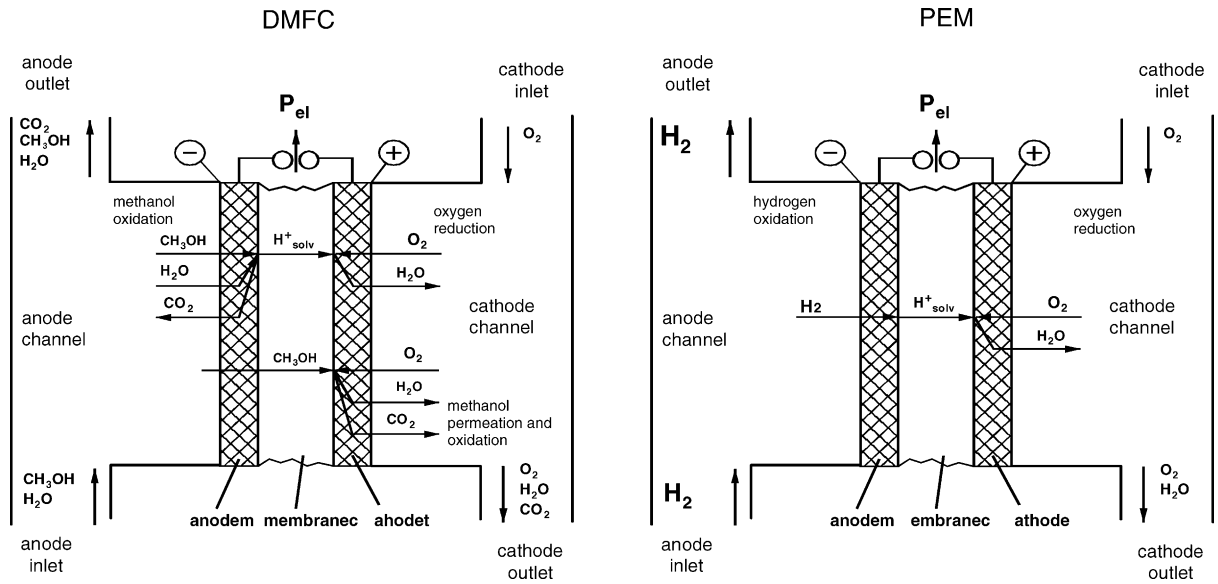| Type	Overall reaction	$-\Delta H^0$ (kJ/mol)	$-\Delta G_0$ (kJ/mol)	E_0 (V)	η_{th} ($\Delta G/\Delta H$)
PEM	$H_2 + 0.5O_2 \rightarrow H_2O_{liquid}$	285.8	237.4	1.229	0.829
DMFC	$1.5O_2 + CH_3OH \rightarrow CO_2 + 2H_2O_{liquid}$	726.3	702.4	1.214	0.967

Fig. 1. Principle of DMFC and PEM fuel cells with proton exchange membranes.
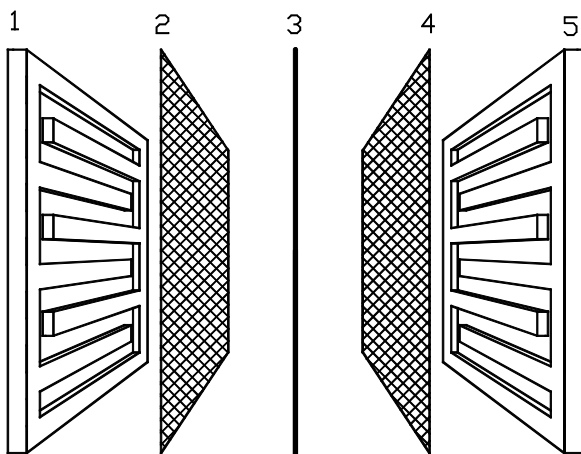

Fig. 2. Membrane fuel cell. 1: anode bipolar plate with flow field for electrical contact and distribution of reactant; 2: anode diffusion layer; 3: catalyst coated membrane; 4: cathode diffusion layer; 5: cathode bipolar plate.

fuel cells we visualized the flow distribution in different combinations of meanders and diffusion layers. In a second step, a model was developed describing the flow processes. The results of parameter studies serve to determine suitable combinations of flow fields and diffusion layers.
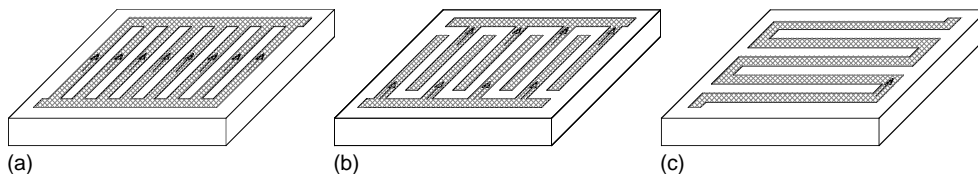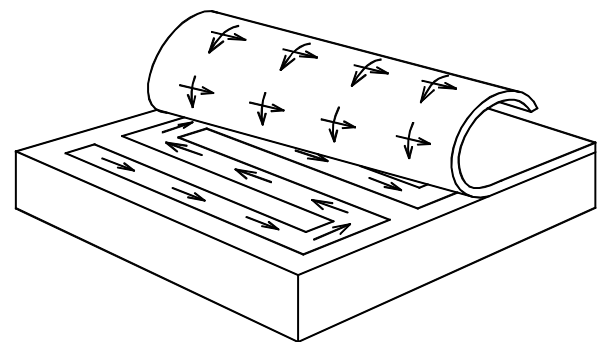

Fig. 4. Scheme of the interaction between the flow field and the diffusion layer. The diffusion layer is in direct contact with the flow field. Due to the pressure gradient in the flow field, there is an additional flow in the diffusion layer which is superpositioned by a flow in the diffusion layer. The resulting overall flow distribution is the sum of both mass flows.

2. Characteristic parameters of flow distribution

This section briefly describes definitions and characteristic parameters of the flow in fuel cells.

2.1. Flow homogeneity

Cell areas supplied with low amounts of reactants are affected by diffusion overvoltages in the electrodes lowering

Fig. 3. Different flow fields for fuel cells. (a) Channel structure; (b) interdigitated structure; (c) meander structure.
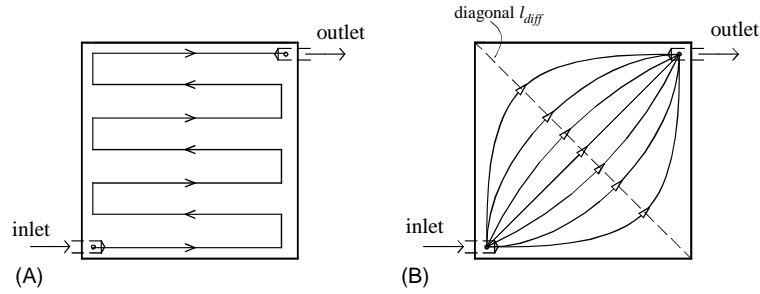
Fig. 5. Boundary cases for the flow distribution in a meander structure combined with a diffusion layer. Case (A) shows an ideal flow through the meander channel. For high permeabilities the flow type (B) can occur where the flow passes only the diffusion layer.

the current density. In the following, parameters characterizing the flow homogeneity are defined.

In a system consisting of a meander structure and a diffusion layer there are two borderline cases. The first assumes low permeabilities of the diffusion layer. Then the overall flow is guided through the meander only. The second borderline case describes a high permeability of the diffusion layer compared to the meander. This results in the total flow going through the diffusion layer. The two boundary cases are shown in Fig. 5.

The mean specific volume flow $\bar{\bar{v}}_{spec}$ is equivalent to the inlet volume flow $\dot{V}$ divided by the cell area A_{cell}. This parameter will be used for the calculation of the flow homogeneity by comparing it with the local flow rates.

By integrating the local volume flow $\dot{V}_{local}^{meander}$ (l/h) over the entire length of the meander channel L_M, the specific volume flow in the meander channel $\bar{v}_{spec}^{meander}$ is obtained as

$$\bar{v}_{spec}^{meander} = \frac{1}{A_{cell}} \frac{1}{L_M} \int_0^{L_M} \dot{V}_{local}^{meander} \, dL_M \tag{2.1}$$

In contrast to the flow in the meander (Fig. 5A), where the flow velocity is always in the same order, the flow velocity in the diffusion layer strongly varies across the electrode area (Fig. 5B). In the region of the inlet and the outlet, the flow cross-section is substantially smaller than, e.g. in the middle of the cell. The total specific flow through the diffusion layer $\bar{v}_{spec}^{diff}$ is obtained by mass conservation:

$$\bar{v}_{spec}^{diff} = \bar{\bar{v}}_{spec} - \bar{v}_{spec}^{meander} \tag{2.2}$$

The fractions χ_M and χ_{diff} are reflecting the ratio of the average flow in both the meander and diffusion layer to the total flow.

$$\chi_M = \frac{\bar{v}_{spec}^{meander}}{\bar{\bar{v}}_{spec}} \quad \text{and} \quad \chi_{diff} = \frac{\bar{v}_{spec}^{diff}}{\bar{\bar{v}}_{spec}} \tag{2.3}$$

Due to mass conservation, the fraction χ_{diff} of the flow passing the diffusion layer is thus:

$$\chi_{diff} = 1 - \chi_M \tag{2.4}$$

In the following we define the flow homogeneity for both the meander and diffusion layer. The ratio of meander flow

to the overall flow as defined in Eq. (2.3) can be used in the same time as an expression for the flow homogeneity ψ_M:

$$\psi_M = \chi_M = \frac{\bar{v}_{spec}^{meander}}{\bar{\bar{v}}_{spec}} \tag{2.5}$$

If the flow is passing only in the meander, the local flow $\dot{V}_{local}^{meander}$ is constant and according to Eq. (2.1) the parameter ψ_M has the value 1.0. If the flow only passes in the diffusion layer the flow takes mainly the shortest connection between cell inlet and outlet. Then, the corners are expected to be less supplied with reactants (Fig. 5) whereas the areas between inlet and outlet are well supplied. This causes the presence of insufficiently and sufficiently supplied areas on the MEA. To take this into account, the maximum value of χ_{diff} is set to 0.5 for the borderline case of the flow passing only in the diffusion layer.

$$\psi_{diff} = \frac{1}{2} \frac{\bar{v}_{spec}^{diff}}{\bar{\bar{v}}_{spec}} \tag{2.6}$$

By using χ_M and χ_{diff} as weighting factors, the overall flow homogeneity ψ results in

$$\psi = \chi_M \psi_M + \chi_{diff} \psi_{diff} \tag{2.7}$$

respectively,

$$\psi = \left(\frac{\bar{v}_{spec}^{meander}}{\bar{\bar{v}}_{spec}} \right)^2 + \frac{1}{2} \left(\frac{\bar{v}_{spec}^{diff}}{\bar{\bar{v}}_{spec}} \right)^2 \tag{2.8}$$

This is a semi-empirical expression valid for a meander flow field combined with a porous diffusion layer. Of course, if the bipolar plate itself is porous like porous carbon materials with a meander structure manufactured inside then the resulting flow can be described equivalently.

The borderline cases are summarized in Table 2 for the two borderline cases mentioned above. Due to insufficient flow supply to the corners the overall homogeneity ψ is 0.5 for the flow passing only in the diffusion layer. In contrast, flow passing only in the meander leads to a overall homogeneity ψ of 1.

Flow homogeneity helps to evaluate different flow fields, but it is not the sole criterion for the evaluation of flow fields

Table 2
Parameters of flow homogeneity for borderline cases

	Flow passing only in the	
	Meander	Diffusion layer
$\bar{v}_{spec}^{diff}/\bar{v}_{spec}$	0	1
ψ_{diff}	0	0.5
$\bar{v}_{spec}^{meander}/\bar{v}_{spec}$	1	0
ψ_M	1	0
ψ (overall homogeneity)	1	0.5

or for a decision whether a flow field is suitable or not. Another important parameter, especially for the cathode of fuel cells, is the pressure drop which requires compressor work reducing the total system power. In general, a flow field is a compromise between flow homogeneity and low pressure drop. In our simulation studies, the pressure drop will be taken into account too.

2.2. Reynold's numbers of the anode and the cathode

An important issue for the flow distribution in the meander/diffusion layer compound is the ratio of the flow conductivity with respect to the drag coefficient of the meander channel and the permeability of the diffusion layer.

Therefore, in a first step, the pressure drop characteristics of the meander and the diffusion layers are determined separately. To avoid too high pressure drops, the meander structure should be operated in the laminar flow regime. The Reynold's number Re is the decisive flow parameter with:

$$Re = \frac{vd_{hyd}}{\nu} = \frac{vd_{hyd}\rho}{\eta} \tag{2.9}$$

with v being the flow velocity and d_{hyd} being the hydraulic diameter. The viscosity can be expressed as a kinematic viscosity ν, which is the dynamic viscosity η divided by the density ρ. $Re < 2300$ indicates the laminar flow. The Re-number can be calculated for the anode of the DMFC which is operated with a liquid methanol/water mixture and for the gaseous cathode of both DMFC and PEM fuel cells.

The stoichiometric flow rates λ_{MeOH} and λ_{air} define the ratio of the reactants fed to the fuel cell to the amount of reactants electrochemically converted. To prevent depletion of methanol at the anode or air at the cathode, the fuel cell is fed with flow rates $\lambda > 1$.

Although the progresses in DMFC development during the last years lead to better performance, the power density is significantly lower than in PEM cells [9]. For a first estimation of the Re-number, the following assumptions are made:

DMFC-anode:

- maximum current density i is 0.4 A/cm^2;
- methanol concentration c_{MeOH} is 1 M;
- the stoichiometric flow rate of the methanol/water;
- mixture λ_{MeOH} is in the range of 3–8;

- the cell area A_{cell} is 100 cm^2.

PEM-cathode:

- maximum current density i is 0.8 A/cm^2;
- the stoichiometric air flow rate λ_{air} is in the range of 1.5–3;
- the cell area A_{cell} is 100 cm^2.

Both flow types are regarded as single phase flows. This is a simplification as the liquid flow of the DMFC anode is influenced by the CO_2-bubble formation especially at high current densities. At the cathode, the influence of the liquid phase is relatively small because the specific volume of the liquid phase is much smaller than the gas phase leaving the geometry of the gas channels unchanged. The velocity v of the air in the meander channel can be calculated from the mass flow using Faraday's law and the geometric parameters of the meander channel. When using N parallel meanders with a cross-sectional area A_M, the total volume flow is distributed homogeneously on the N meander channels.

$$v = \frac{\dot{V}}{A_M N} \quad \text{with}$$

$$\dot{V} = \frac{I}{4F}\frac{1}{x_{O_2}}\lambda_{air}\frac{M_{air}}{\rho_{air}} \quad \text{for the cathode} \quad \text{and}$$

$$\dot{V} = \frac{I}{6F}\frac{1}{c_{MeOH}}\lambda_{MeOH}\frac{m}{1000l} \quad \text{for the DMFC anode} \tag{2.10}$$

In the equation for the anodic volume flow the term $I/6F$ is the consumption of methanol according to Faraday's law. The anode of the DMFC is fed with a methanol/water solution which has a concentration c_{MeOH} expressed in mol/l. Typical concentrations are in the range from 0.2 to 1 M depending on the current density, the operating temperature and membrane properties as thickness, methanol diffusivity and other parameters [10,11]. To prevent methanol depletion in the channels, the methanol/water mixture is fed with a stoichiometric flow rate $\lambda_{MeOH} > 1$. In comparison to the cathode, this flow rate can be significantly higher as the energy demand for the methanol/water pump is generally lower than that for the air compressor. A typical range for λ_{MeOH} is 4–10.

Geometric parameters of the meander channel are the height h_M and the width b_M. The cross-sectional area A_M of each meander channel is

$$A_M = h_M b_M \tag{2.11}$$

The hydraulic diameter d_{hyd} of the meander channel is calculated by the cross-sectional area A_M and its circumfence U_M:

$$d_{hyd} = \frac{4A_M}{U_M} = \frac{4b_M h_M}{2(b_M + h_M)} \tag{2.12}$$

By combining the Eqs. (2.10) and (2.12), Re can be expressed for both the anode the cathode with N representing

Table 3
Re-number for different operating conditions

Type	Temperature in (°C)		
	25	50	100
Liquid DMFC-anode ($\lambda_{MeOH} = 3\text{--}8$, $I = 40\,A$)	232–618	534–1425	703–1874
Gaseous PEM-cathode ($\lambda_{air} = 1.5\text{--}3$, $I = 80\,A$)	989–1979	935–1871	834–1667

Dimensions of the meander channel: $b_M = 1\,mm$, $h_M = 1\,mm$. Methanol concentration: 1 M. Active cell area: 100 cm². One meander channel ($N = 1$).

the number of meander channels:

$$Re = 2\dot{V}\frac{1}{N}\frac{1}{v}\frac{1}{b_M + h_M} \tag{2.13}$$

The resulting *Re*-numbers for the DMFC anode and the PEM/DMFC cathode are summarized in Table 3. It can be seen that the *Re*-number is in all cases smaller than 2300. At high current densities and higher air flows, the *Re*-numbers are in the range 1600–2000. An additional increase in air flow could turn the flow into turbulence. This is an indication that at high current densities and high air flow rates the total flow should be divided on at least two channels to avoid turbulent flow.

2.2.1. Pressure drop in the meander

The *Re*-number calculated above is an important parameter for calculating the pressure drop in the meander. In general the meander structure consists of straight sections which are connected in the corners where the flow is redirected. The pressure drop in the straight section of the meander is

$$\Delta p_v = \tau \frac{\Delta l}{d_{hyd}}\frac{\rho}{2}v^2 \tag{2.14}$$

with τ being the drag coefficient for laminar flow:

$$\tau = \varphi\frac{64}{Re} = \varphi\frac{64\mu}{\rho d_{hyd}v} \tag{2.15}$$

The correction factor φ fits the drag coefficient τ to the geometry of the specific hydraulic diameter. For the quadratic cross-section of the channels used in the experiments φ is 0.88 [12]. In addition to the pressure drop in the meander channel, the redirection of the flow in the corners of the meander causes further pressure drops. They can be calculated by

$$\Delta p_{redirect} = \zeta\frac{\rho}{2}v^2 \tag{2.16}$$

with ζ being in the range of 1–2 depending on the geometry of the corners (square-edged or rounded).

3. Experimental

3.1. Permeability measurements of the diffusion layer

To determine the permeability *k* of the diffusion layers the experimental set-up shown in Fig. 6 was used. The material sample is mounted between two endplates made of perspex. One endplate is provided with concentric inlet and outlet channels. The volume flow $\dot{V}$ measured by a mass flow meter is pressed through these concentric channels and the pressure drop Δp is detected. A defined thickness *s* of the diffusion layer can be adjusted by distance spacers which can be mounted additionally between the endplates which servers to investigate different compression stages of the diffusion layers.

The experimental set-up is suitable for measurements with air and with water. When using water, the air mass flow
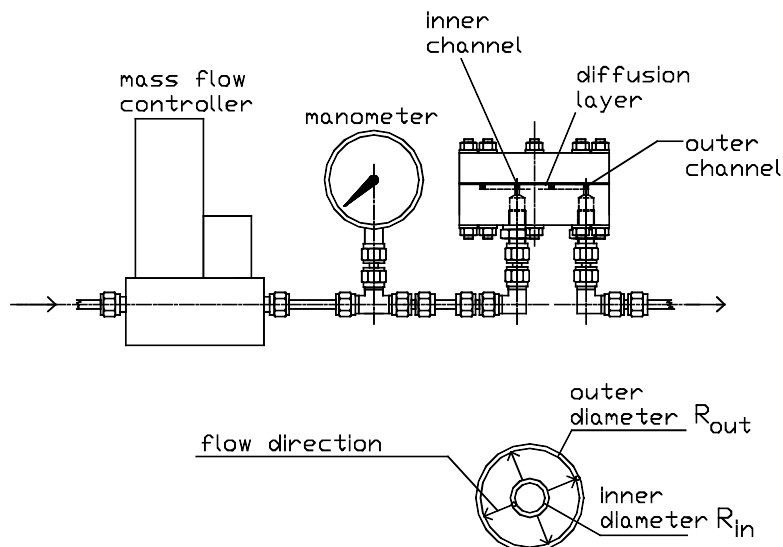

Fig. 6. Experimental set-up for the determination of the pressure drop of diffusion layers.

controller is replaced by a pump and the volume flow is measured by weighing the outgoing water stream.

The flow velocity passing the porous diffusion layer can be calculated using Darcy's law:

$$v_{\text{diff}} = -\frac{k}{\eta}\nabla p \tag{3.1}$$

The measured volume flow $\dot{V}$ is

$$\dot{V} = -2\pi r \frac{k}{\eta}\frac{dp}{dr}s \tag{3.2}$$

By integration of Eq. (3.2)

$$\frac{\dot{V}}{2\pi s}\int_{R_{\text{in}}}^{R_{\text{out}}}\frac{dr}{r} = -\frac{k}{\eta}\int_{p_{\text{in}}}^{p_{\text{out}}}dp \tag{3.3}$$

the permeability coefficient k is obtained with $p_{\text{in}} - p_{\text{out}}$ being the pressure drop Δp:

$$k = \frac{\dot{V}}{\Delta p}\frac{\eta}{2\pi s}\ln\left(\frac{R_{\text{out}}}{R_{\text{in}}}\right) \tag{3.4}$$

The permeability k is a geometric parameter expressed in the unit m^2.

The diffusion layers to be measured were manufactured in house. To obtain high power densities an optimized mass transport to the catalyst region is necessary. The preparation of the diffusion layers and the influence of porosity on the power density is one of the most important topics and has been investigated in detail [13–18]. In our experiments both the DMFC-anode and PEM-cathode gas diffusion layers were prepared by mixing carbon powder with finely-dispersed PTFE. With regard to the different mass transport properties of the electrodes, the PTFE content is in the range of 15% in the anode to provide a sufficient transport of liquid methanol and water to the catalyst layer and 40% in the cathode for an improved hydrophobicity for

Table 4
Influence of the height s and the medium (water/air) on the permeability of a diffusion layer

Gap width s (mm)	Permeability k (m^2)	
	Air	Water
0.2	1.05E−11	–
0.3	1.41E−11	3.34E−12
0.4	1.62E−11	6.60E−12
0.5	3.33E−11	2.34E−11

At the same time the height s indicates the compression state. Structural data are the same as in Fig. 7.

product water removal [16]. The mixture was then applied to carbon cloth with loading of ca. 5 mg/cm^2 with a subsequent sintering process at 350 °C. An important difference between anode and cathode diffusion layers is the pretreatment of the carbon cloth: in the case of anode diffusion layers the carbon cloth is untreated, whereas for cathode diffusion layers the carbon cloth is hydrophobized by PTFE with a loading of ca. 1 mg/cm^2. Fig. 7 shows the measured pressure drop as a function of the volume flow for different gaps widths s. The pressure drop is nearly proportional to the flow rate except for the case of the widest gap (0.5 mm) which is in the same order as the thickness of the diffusion layer. This can be explained by the formation of bypass flows between endplates and diffusion layer if the endplates of the measuring device (Fig. 6) are not sufficiently pressed on the diffusion layer. Consequently, at smaller gap widths with a better contact, this effect cannot be further observed.

Although the permeability is a geometric property of the diffusion layer, it is different for water and for air as shown in Table 4. Due to the surface tension of water, the pores of the diffusion layer become filled, changing the pore geometry and decreasing the permeability. During the operation of a fuel cell, the diffusion layers are partially wetted, therefore
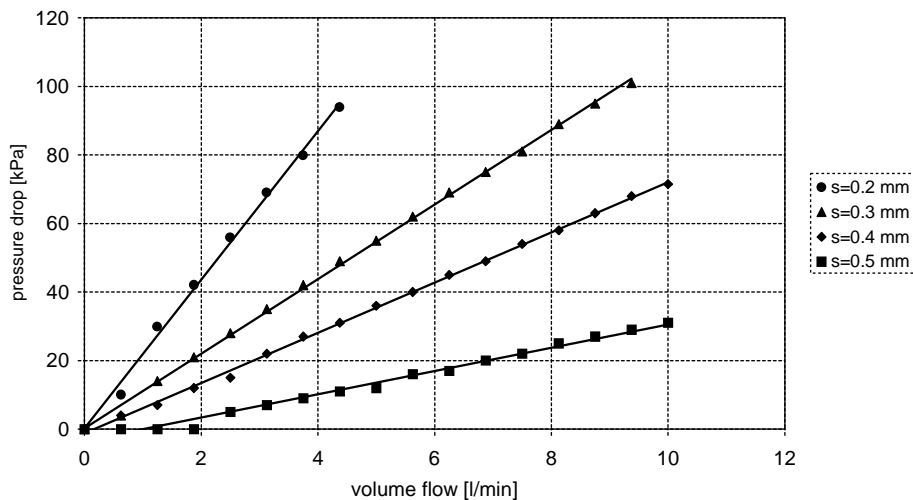

Fig. 7. Pressure drop with variation of the compression of the diffusion layer. In uncompressed state ($s = 0.5$ mm) the pressure drop is ca. eight times smaller than in the fully compressed state ($s = 0.2$ mm). Composition of the diffusion layer: 30% PTFE, 70% XC72 on hydrophobized carbon cloth. Measurements made in air.

Table 5
Influence of the PTFE-content on the permeability of the diffusion layers

PTFE content (%)	Permeability k (m^2)		Ratio (k_{air}/k_{water})
	Air	Water	
15 (CC untreated)	1.36E−11	2.86E−12	4.76
20 (CC untreated)	1.68E−11	6.22E−12	2.70
30 (CC teflonized)	1.41E−11	3.34E−12	4.22
40 (CC teflonized)	3.73E−11	9.48E−12	3.93

The gap width is 0.3 mm in all cases. CC: carbon cloth.

the real permeability coefficient is expected to be somewhere between the two borderline cases.

The PTFE content influences both the permeabilities for air and water as shown in Table 5. Roughly speaking, an increasing PTFE content leads to a higher permeability. Regarding the water, this is an unexpected effect as one would assume lower permeabilities due to the increased hydrophobicity. The ratio (k_{air}/k_{water}) is always in the range between 2.5 and 5 and does not show any dependency on the PTFE content of the carbon powder/PTFE mixture. This phenomenon may be explained by the slightly different preparation of the diffusion layers and has not further been examined.

3.2. Flow visualization

For the flow visualization, we used the test equipment shown in Fig. 8 which is similar to that described in [19,20]. It consists mainly of a pump and a flow field made of perspex. The flow field is designed in the same way as the plates of our laboratory fuel cells. The size of the flow field is 100 mm × 100 mm. The pressure loss through the cell is monitored by means of two simple manometers. To ensure a better visualization, diffusion layers with defined geometries made of polyethylene sheets (Fig. 9) were used. In two polyethylene sheets with a thickness of 80 μm, channels with a defined geometry are cut (Fig. 9a). The resulting geometry of the two sheets is a grid structure as shown in Fig. 9b. For a channel width of 0.5 mm and a channel distance of 5 mm we measured a permeability k of 5.06E−11 m^2. This is in the
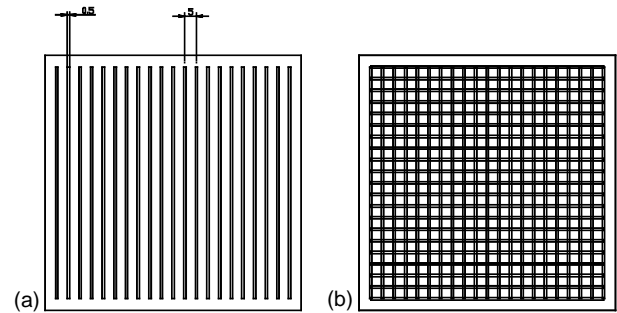

Fig. 9. Example of model diffusion layers made of polyethylene sheets with defined geometry (thickness 80 μm, channel width 0.5 mm, channel distance 5 mm). Two sheets (a) positioned above each other as shown in (b) form a defined grid structure with a permeability k of 5.06E−11 m^2. This is in the range of real diffusion layers (Table 4).

same order of magnitude as for the real diffusion layers (see Table 4). Furthermore, the usage of model diffusion layers extends the permeability range to be tested. The pump of the test rig can be switched between pure water and colored water. A video camera serves to record the resulting flow front.

A comparison of the flow distribution for two different model diffusion layers is shown in Fig. 10. The thick lines show the flow front—determined each 2 s—after analysis of the video sequences. The flow distribution shown in the left of Fig. 10 is homogeneous, the whole active area is covered by the flow which takes approximately 16 s. Only in the left and right side of the flow field the flow has a slight tendency towards the cell outlet which is not very important as this effect is limited only to a small part of the overall active area. In contrast, the higher permeability of the diffusion layer shown in the right part of Fig. 10 leads to an inhomogeneous flow distribution. In comparison to the left picture, it takes the flow ca. 50% longer (24 s) to cover the whole area. There are two preferred directions of the flow: the first one is from the flow inlet following the left and the upper border of the active area, whereas the second preferred direction is the path following the bottom and the right border. As a consequence, the central areas of the flow field are depleted. This is an important observation as consequently the local stoichiometric flow rate in the central area is much lower
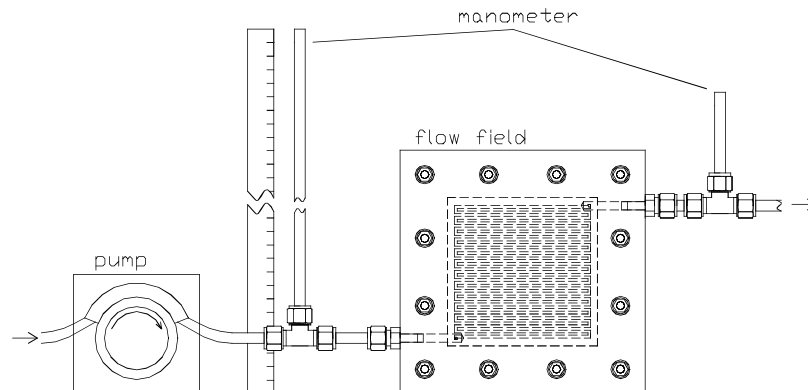

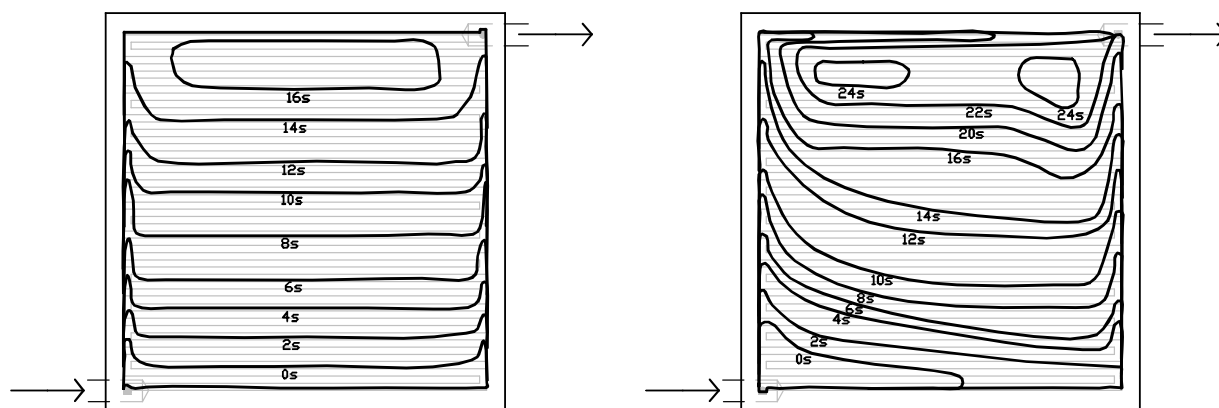Fig. 8. Test equipment for flow visualization.

Fig. 10. Flow visualization for different combinations of meander flow fields and diffusion layers. The curves in the flow field indicate the flow propagation velocity. Meander channel: 2 mm × 2 mm, active area: 100 cm². Permeabilities of the diffusion layers: 2.75E−11 m² (left) and 3.32E−9 m² (right). Flow rate in each case 1.44 l/h water with traces of red ink. Temperature: 25 °C.

causing lower local current densities in real fuel cells. As an estimation based on the video sequences, the flow in the central area is only the half of the flow in the border areas. For example, after 9 s approximately the half of the whole cell area is covered for the low permeability of the diffusion layer (2.75E−11 m², left part of Fig. 10), whereas after the same time the high permeability lowers the coverage to the area after the same time by approximately 50% to a amount of approximately only a quarter.

In the following chapter, we investigate in more detail the influence of design parameters as flow field size, meander geometry, number of meanders and permeability of the diffusion layers on the flow homogeneity.

3.3. Cell testing of laboratory scale DMFC

In addition to the cells described above, DMFC laboratory cells using two different flow fields shown in Fig. 11 were tested. The meander flow field shown in the left consists of channels and ribs with a width of 3 mm each and a height of 0.8 mm. An additional channel structure with a thickness of 0.3 mm is positioned above the meander flow field to provide reactant flow also towards the contact area between membrane electrode assembly (MEA) and flow field. For flow visualization purposes, this metallic channel structure is replaced by polyethylene sheets with a suitable thickness. On the right, the flow distribution in a grid structure is visualized. The grid structure is also provided with an additional channel structure. It can be clearly seen that the combination of the meander structure with the additional channel structure—which is equivalent to an additional porosity—causes an inhomogeneous flow especially in the middle of the cell. The main flow is concentrated on both sides of the flow field leaving the upper middle area of the cell unsupplied. The active area of each test cell is 25 cm².

The flow in the grid structure is much more homogeneous. On the photograph it can be seen that the flow covers the whole area of the cell.
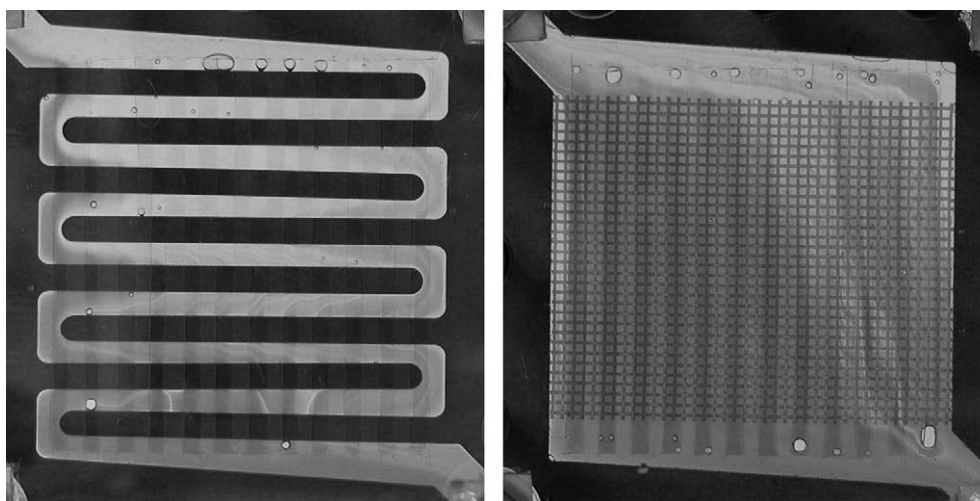

Fig. 11. Comparison of DMFC flow fields. (Left) Meander flow field; (right) grid flow field with internal manifolds. Both flow structures are combined with a thin (0.3 mm) channel structure which is positioned directly on the meander, respectively, the grid.

3.4. Manufacturing of membrane electrode assemblies (MEAs)

The MEAs used for the experiments were fabricated in-house. The membrane electrode assembly (MEA) for our DMFC test cells consists of a polymer membrane (Nafion 117) with anode and cathode catalyst layers and carbon gas diffusion layers. In the following, the main manufacturing steps of the MEAs are briefly described. Details are given elsewhere [21,22].

Both the anode and cathode gas diffusion layers were prepared by mixing carbon powder with finely-dispersed PTFE as described in detail above. With regard to the different mass transport properties of the electrodes, the PTFE content is 10% in the anode to ensure a sufficient transport of liquid methanol and water to the catalyst layer and 40% in the cathode for an improved hydrophobicity for product water removal.

The anodic catalyst loading is 4 mg/cm^2 carbon-supported Pt/Ru with an atomic ratio of 1:1; cathodic loading is 4 mg/cm^2 Pt-black. The cathode catalyst layer was prepared by a spraying method, whereas the anode was prepared by a decal method, which is based on three steps:

1. mixing the catalyst with a Nafion solution with subsequent application on a PTFE foil;
2. drying process at 80 °C;
3. hot-pressing of the catalyst layer onto the membrane at 130 °C, 0.5 kN/cm^2, 5 min;
4. removal of the PTFE-foil.

In contrast to the anode catalyst layer the cathode was prepared by the application of the catalyst on the diffusion layer with subsequent hot-pressing onto the membrane.
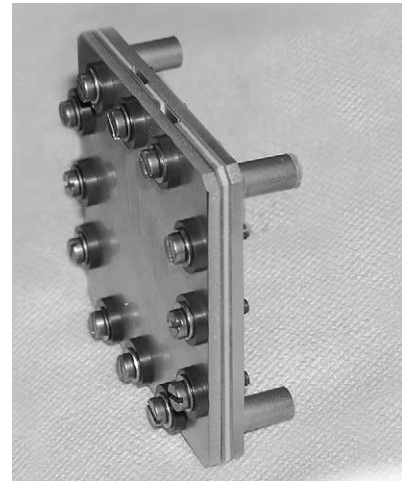

Fig. 12. DMFC single cell with an active area of 25 cm^2. The end plates are made of stainless steel.

3.5. Flow distribution versus power density

The MEAs were assembled into a test cell shown in Fig. 12. For the evaluation of the flow fields, the voltage/current density characteristics were investigated. Air was used as oxidant at ambient pressure at constant 1 l/min. The methanol concentration was set to 1 M at a volume flow of 540 ml/h. By means of a preheater, the methanol/water mixture (anode inlet) was set to a defined temperature. In addition, the anode outlet temperature was measured. The two temperatures can be different due to heat generation in the cell and due to water evaporation in the cathode. At anode temperatures above 60 °C, the anode outlet temperature is significantly lower than the anode inlet temperature
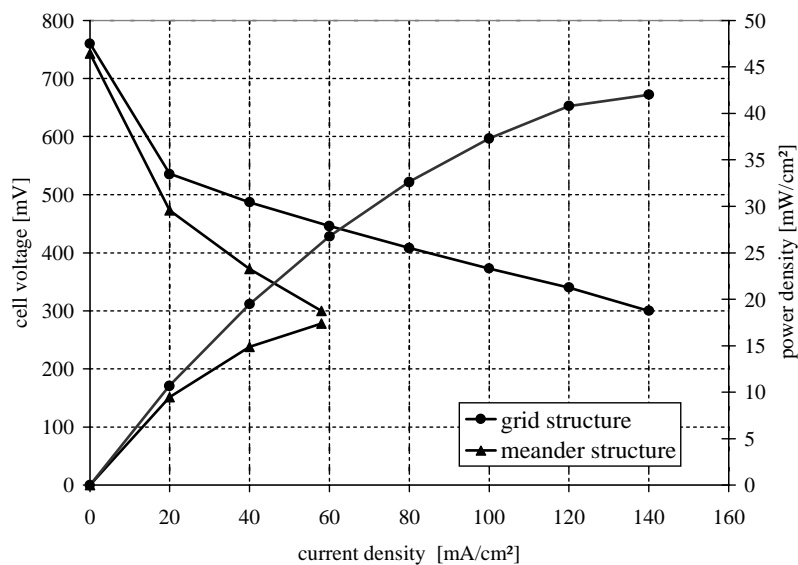

Fig. 13. Comparison of cell voltage/current density characteristics of laboratory scale DMFC single cells with different flow fields. Anode feed temperature: 80 °C, volume flow 540 ml/h. Anode outlet temperature: 54 °C (meander); 64 °C (grid structure). Methanol concentration 1 M. Air flow rate 1 l/min at ambient pressure.
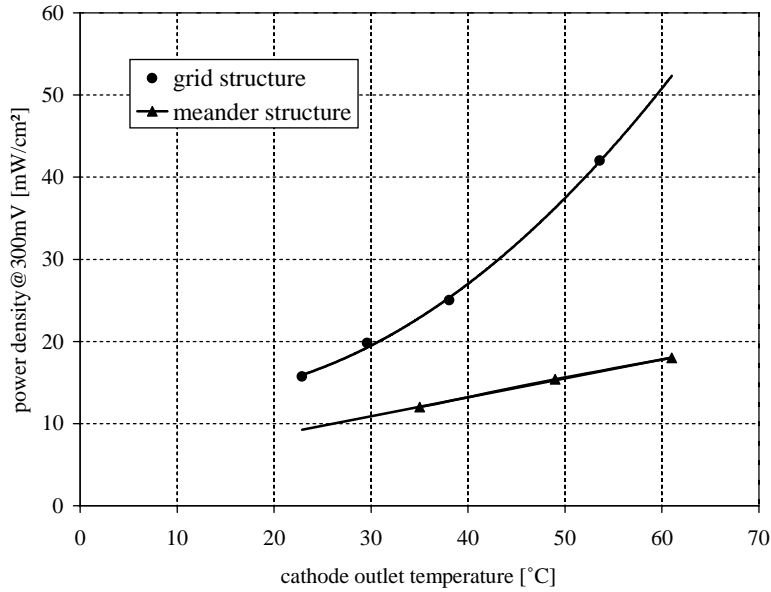
Fig. 14. Influence of the temperature on the power density for different flow fields. Anode volume flow: 540 ml/h; methanol concentration: 1 M; cathode volume flow: 1 l/h air at ambient pressure.

as the water evaporation in the cathode chamber dominates the heat balance.

Fig. 13 shows the cell voltage/current density characteristics for the two different flow fields shown above. Compared to the grid structure, the power density obtained with the combined meander/channel structure is in the order of only 40%. Due to the higher power density, the temperature in the grid structure is approximately 10 °C higher than in the meander/channel structure even if both cells are provided with the same inlet temperature. For a better comparison of the two cell flow fields, the power density is shown as a function of the cathode outlet temperature in Fig. 14. The gap in the two power densities grows with rising temperature. This is an indication for mass transport problems. An increase in the power density is accompanied by an increasing reactant demand in the whole cell area which can not be fulfilled by the meander/channel flow field causing diffusion overvoltages.

4. Simulation study

The interaction of the meander and the diffusion layer was analyzed by simulation studies. The program is written in a Fortran 95 code. The simulation model is based on the finite volume element method. In the laminar flow regime, the meander structure can be regarded as a series of discrete resistances, whereas the diffusion layer is an additional resistance matrix (Fig. 15).

The simulation is based on the discretization of the in Chapter 2 defined mass transport equations similar to the method described in [19]. For each volume element, the equations for the mass conservation are solved, i.e. the sum of the incoming and outgoing volume flows must be zero:

$$\sum \dot{V}_{in,out} = 0 \quad \text{for each volume element} \tag{4.1}$$

The volume elements are connected by the channels and the diffusion layers. The incoming and outgoing volume
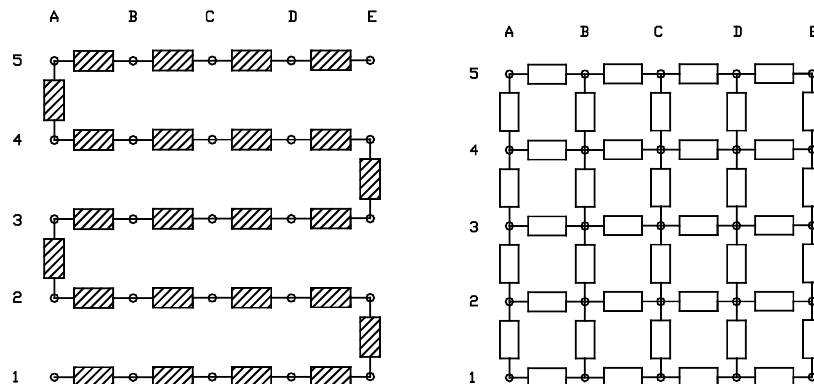

Fig. 15. Model of flow resistance in meander flowfield (left) and diffusion layer (right).

flows depend on the local pressure gradient and the local conductivity. For the laminar flow regime, the resulting local pressure gradient is proportional to the local volume flow which leads to a system of linear equations for the mass conservation which can be expressed as:

$$\bar{\bar{L}}\bar{p} = \bar{C} \tag{4.2}$$

The coefficient matrix $\bar{\bar{L}}$ contains the coupling conductivities of each point with the adjacent volume elements of the discretized model region. The overall conductivity between two points of the grid is a superposition of the conductivity of the meander and the diffusion layer and is calculated using Eq. (2.14) for the meander and Eq. (3.1) for the
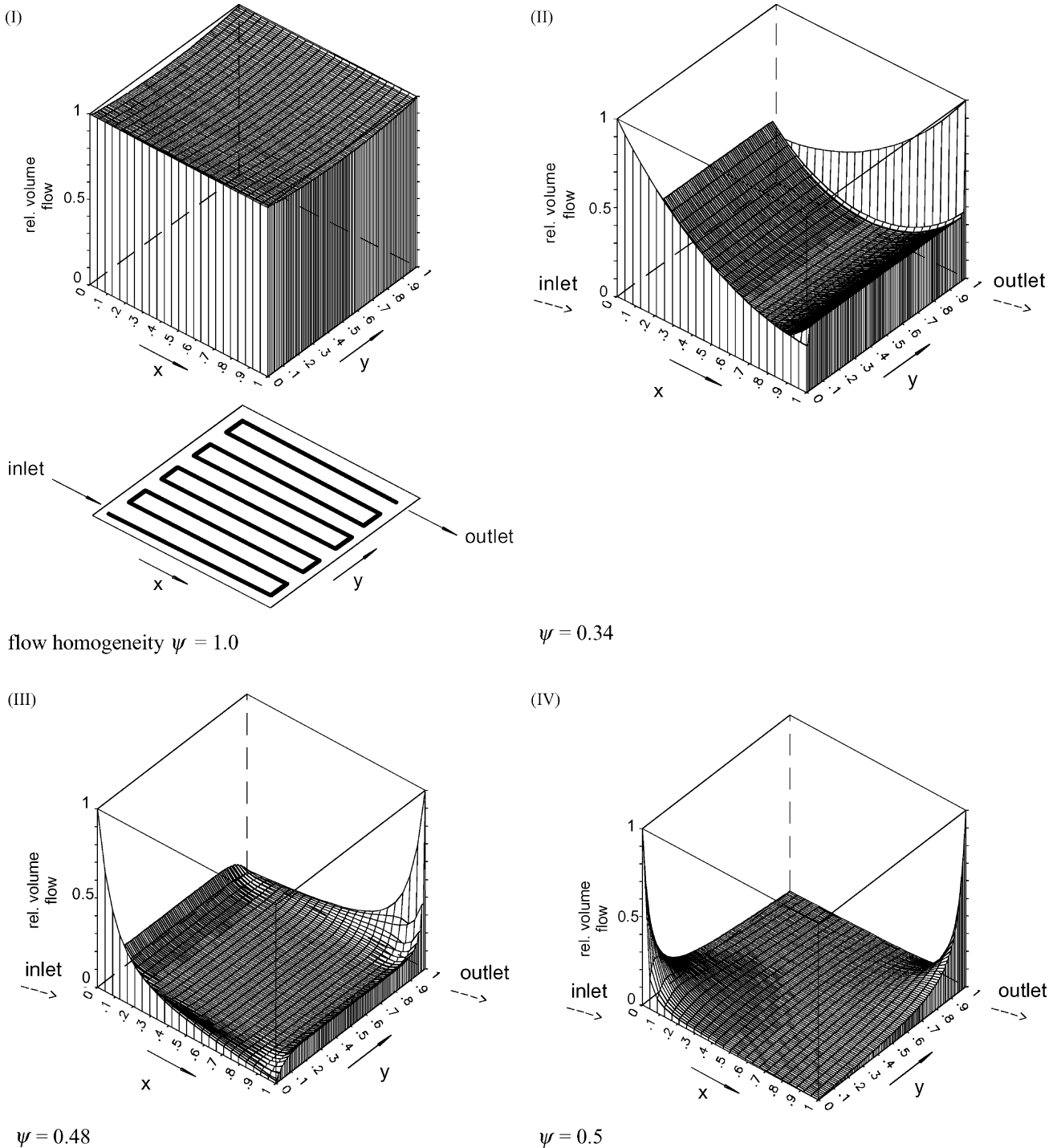

Fig. 16. Flow distribution for different permeabilities of the diffusion layer. The flow distribution is calculated for a cell area of $200\,\text{mm} \times 200\,\text{mm}$ and a $1\,\text{mm} \times 1\,\text{mm}$ meander. Permeabilities: (I) 2.2E−14 m^2; (II) 4.6E−12 m^2; (III) 4.6E−10 m^2; (IV) 4.6E−4 m^2. Thickness of the diffusion layer in all cases: 0.4 mm.
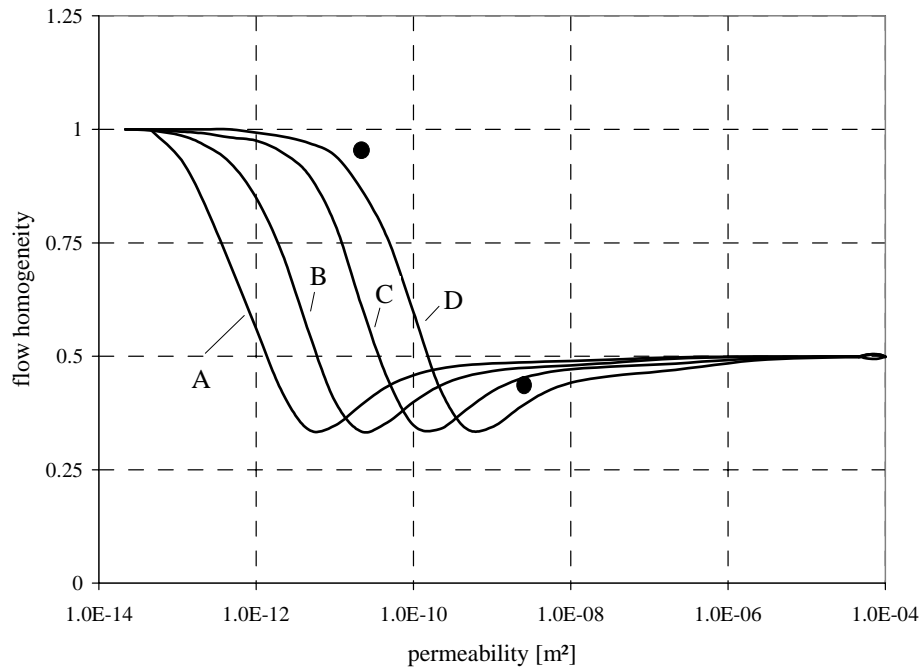
Fig. 17. Influence of the permeability of the diffusion layer on the flow homogeneity for different cell geometries. Results based on simulation. The dots represent the correlation to the experimentally tested flow field geometries (see Fig. 10). (A) Cell area 200 mm × 200 mm, meander cross-section 1 mm × 1 mm. (B) Cell area 100 mm × 100 mm, meander cross-section 1 mm × 1 mm. (C) Cell area 200 mm × 200 mm, meander cross-section 2 mm × 2 mm. (D) Cell area 100 mm × 100 mm, meander cross-section 2 mm × 2 mm.

diffusion layer. In a first step the vector $\bar{p}$ containing the local pressures is calculated by solving (4.2). $\bar{C}$ comprises the local sources and sinks as, e.g. the channel in- and outlets. Once the vector $\bar{p}$ is calculated, the local volume flow can be determined in a second step by multiplying the local pressure gradient by the local conductivity. Typically, a system of 25 × 25 elements has been used for calculation.

4.1. Simulation results

Results of the simulation studies are presented in Fig. 16. The inlet volume flow is taken as a reference and set to 1.0. Across the cell area the relative volume flow varies according to the permeability of the diffusion layer resulting in a varying overall flow homogeneity ψ as defined in Eq. (2.7). Fig. 16, it shows the orientation of the meander channel and the flow inlet and outlet. As expected, low permeabilities of the diffusion layer lead to an overall flow mainly through flow paths in the diffusion layer.

Fig. 17 summarizes the influence of the permeability of the diffusion layer for four different cell geometries using the simulation. The flow homogeneity ψ is calculated according to Eq. (2.8). The thickness of the diffusion layer was assumed to be 0.4 mm in all cases. The effects due to the compression of the diffusion layer, e.g. by cell assembling or swelling of the membrane, are not taken into account for simplification purposes. Consequently, the permeabilities assumed in the simulation studies can be 2–3 times higher compared to real fuel cells (Table 4), i.e. in real

systems the curves shown in Fig. 17 are slightly shifted to the right.

4.2. Correlation to flow experiments

The flow experiments performed in the experimental section can be correlated to the simulation. The geometry of the test cell with a 2 mm × 2 mm meander described in Fig. 10 complies with the simulation results in Fig. 17, curve D, for both permeabilities of the diffusion layer. Using the lower permeability of 2.75E−11 m^2, the resulting flow is mainly in the meander. This is an observation for both the experiment and the simulation. As stated above, the flow has only in the left and right side of the flow field a tendency directly to the cell outlet. For this case the calculated homogeneity is in the range of 0.85. The higher permeability of 3.32E−9 affects the flow homogeneity significantly. Again, both simulation and experiment show less flow homogeneity which is estimated to be less than 0.5 for the experimental flow visualization. The estimation is based on the time necessary to cover selected parts of the flow field as well as on the estimation of local flow velocities.

5. Conclusion

The flow distribution in fuel cells has an important influence on the power density. Due to additional flow paths offered by the diffusion layer, even a meander structure can

inhomogeneously distribute the reactants across the flow field area. The flow homogeneity can be calculated in principle by integrating the local flow velocities across the whole cell area. Borderline cases are: (a) flow passing only in the meander channel, (b) flow passing only in the diffusion layer. The latter case is accompanied by a worse flow homogeneity approximately a half of that of the former. To avoid depletion of reactants in specific regions of the cell, the geometry of the meander should be chosen with regard to the permeability of the diffusion layers. Unsuitable combinations of meander geometry and diffusion layer properties lead to even lower flow homogeneities compared to the flow passing only in the diffusion layer. High permeabilities require meander structures with low pressure losses, otherwise the flow homogeneity decreases. The effects obtained by simulation studies have been proven by flow experiments with water and ink. Experiments using DMFC laboratory cells showed a significant influence of the flow distribution on the power density.

References

[1] X. Ren, P. Zelenay, S. Thomas, J. Davey, S. Gottesfeld, J. Power Sources 86 (2000) 111.
[2] A. Kindler, T.I. Valdez, C. Cropely, S. Stone, Electrochem. Soc. Proc. 4 (2001) 231.
[3] H. Dohle, H. Schmitz, T. Bewer, J. Mergel, D. Stolten, J. Power Sources 106 (2002) 313.
[4] T.V. Nguyen, J. Electrochem. Soc. 143 (1996) L103.
[5] A.S. Arico, V. Baglio, P. Creti, V. Antonucci, in: Proceedings of the 2000 Fuel Cell Seminar, Portland, Oregon, 30 October to 2 November 2000, pp. 75–78.
[6] H. Dohle, T. Bewer, R. Neitzel, J. Mergel, D. Stolten, in: Proceedings of the 2000 Fuel Cell Seminar, Portland, Oregon, 30 October to 2 November 2000, pp. 130–135.
[7] J.C. Amphlett, B.A. Peppley, E. Halliop, et al., J. Power Sources 96 (2001) 204.
[8] K. Scott, P. Argyropoulos, W.M. Taama, J. Power Sources 79 (1999) 169.
[9] S. Thomas, X. Ren, S. Gottesfeld, Electrochim. Acta 47 (2002) 3741.
[10] H. Dohle, J. Divisek, R. Jung, J. Power Sources 86 (2000) 469.
[11] K. Scott, P. Argyropoulos, W.M. Taama, S. Kramer, K. Sundmacher, J. Power Sources 83 (1999) 204.
[12] I.E. Idelchick, Handbook of Hydraulic Resistance, CRC Press, Florida, 1994.
[13] C.S. Kong, D.Y. Kim, H.K. Lee, Y.G. Shul, T.H. Lee, J. Power Sources 108 (2002) 185.
[14] D. Bevers, M. Wohr, K. Yasuda, K. Oguro, J. Appl. Electrochem. 27 (1997) 1254.
[15] L. Giorgi, E. Antolini, A. Pozio, E. Passalacqua, Electrochim. Acta 43 (1998) 3675.
[16] L.R. Jordan, A.K. Shukla, T. Behrsing, N.R. Avery, B.C. Muddle, M. Forsyth, J. Power Sources 86 (2000) 250.
[17] M. Uchida, Y. Aoyama, N. Eda, A. Ohta, Electrochem. Soc. 142 (1995) 4143.
[18] J. Nordlund, G. Lindbergh, J. Electrochem. Soc. 149 (2002) 1107.
[19] H.K. Versteeg, W. Malalasekera, An Introduction to Computational Fluid Dynamics: The Finite Volume Method, Longman, Harlow, 1995.
[20] C. Bengoa, A. Montillet, P. Legentilhomme, J. Legrand, J. Appl. Electrochem. Soc. 27 (1997) 1313.
[21] X. Ren, W. Henderson, S. Gottesfeld, Electrochem. Soc. 144 (1997) 267.
[22] A. Havránek, K. Klafki, K. Wippermann, in: Proceedings of the 1st European Polymer Electrolyte Fuel Cell Forum, Luzern/Switzerland, 2–6 July 2001, p. 221.